

Chemically Addressable Perovskite Nanocrystals for Light-Emitting Applications

Haizhu Sun, Zhenyu Yang, Mingyang Wei, Wei Sun, Xiyan Li, Shuyang Ye, Yongbiao Zhao, Hairen Tan, Emily L. Kynaston, Tyler B. Schon, Han Yan, Zheng-Hong Lu, Geoffrey A. Ozin, Edward H. Sargent,* and Dwight S. Seferos*

Whereas organic–inorganic hybrid perovskite nanocrystals (PNCs) have remarkable potential in the development of optoelectronic materials, their relatively poor chemical and colloidal stability undermines their performance in optoelectronic devices. Herein, this issue is addressed by passivating PNCs with a class of chemically addressable ligands. The robust ligands effectively protect the PNC surfaces, enhance PNC solution processability, and can be chemically addressed by thermally induced crosslinking or radical-induced polymerization. This thin polymer shield further enhances the photoluminescence quantum yields by removing surface trap states. Crosslinked methylammonium lead bromide (MAPbBr₃) PNCs are applied as active materials to build light-emitting diodes that have low turn-on voltages and achieve a record luminance of over 7000 cd m⁻², around threefold better than previous reported MA-based PNC devices. These results indicate the great potential of this ligand passivation approach for long lifespan, highly efficient PNC light emitters.


Earth-abundant organometallic-halide-based perovskites are an exciting class of optoelectronic materials with unprecedented growth in performance in a range of applications. For example,

Prof. H. Sun, Dr. W. Sun, S. Ye, Dr. E. L. Kynaston, T. B. Schon,
Dr. H. Yan, Prof. G. A. Ozin, Prof. D. S. Seferos
Department of Chemistry
University of Toronto
80 St. George Street, Toronto, Ontario M5S 3H6, Canada
E-mail: dseferos@chem.utoronto.ca

Prof. H. Sun
College of Chemistry
National & Local United Engineering Laboratory for Power Batteries
Northeast Normal University
5268, Renmin Street, Changchun 130024, P. R. China

Dr. Z. Yang, M. Wei, Dr. X. Li, Dr. Y. Zhao, Dr. H. Tan, Prof. E. H. Sargent
The Edward S. Rogers Department of Electrical and
Computer Engineering
University of Toronto
10 King's College Road, Toronto, Ontario M5S 3G4, Canada
E-mail: ted.sargent@utoronto.ca

Dr. Y. Zhao, Prof. Z.-H. Lu
Department of Materials Science and Engineering
University of Toronto
184 College Street, Toronto, Ontario M5S 3E4, Canada

 The ORCID identification number(s) for the author(s) of this article can be found under <https://doi.org/10.1002/adma.2017011153>.

DOI: 10.1002/adma.2017011153

perovskite solar cells have made tremendous progress in power conversion efficiency, recently achieving a certified value of 22.1%, which is comparable to mature thin-film technologies.^[1] The intrinsic physical properties of halide-based perovskites, such as their low defect density, excellent charge transport properties, and high photoluminescence quantum yield (PLQY), have also enabled great advances in light-emitting applications such as photodetectors,^[2,3] lasers,^[4,5] and light-emitting diodes (LEDs).^[6–17] Similar to the performance gains in perovskite solar cells, intense research in the use of perovskites for light-emitting applications has led to the rapid improvement of perovskite-based LEDs. In just a few years, devices have made incredible progress in their external quantum efficiency (EQE) from

<1% in 2014^[6] to over 10% in 2016,^[13,18] highlighting the excellent promise of perovskites for applications in light emission.

Well-balanced charge injection and efficient radiation recombination in the active material are key parameters for high-performance LEDs.^[19] The strong correlation between material properties and device performance is also valid for perovskite-based devices, where the exciton dissociation in the emissive material (i.e., perovskite crystalline film) is much more favorable than other materials (e.g., quantum dots and semiconductor organic molecules).^[12,20] Well-defined quantum well structures, such as perovskites with reduced structural dimensions^[11,13,21,22] and perovskite nanocrystals (PNCs),^[23–25] effectively minimize exciton dissociation and enhance radiative recombination. For instance, Yuan et al. designed perovskite energy funnels with nanosized dimensions and successfully obtained highly efficient LEDs with EQEs over 8%.^[11] Wang et al. achieved a record EQE of 11.7% by using the similar energy funnels.^[13] Cho et al. fabricated perovskite-based LEDs with an efficiency similar to organic LEDs by reducing the exciton diffusion length of the emissive layer.^[26] These investigations indicate that the fabrication of perovskite-based materials with reduced dimensions (e.g., in the nanometer range) is an effective method to further improve the performance of LEDs based on these materials. Therefore, it is significant to design and synthesize brighter and more stable PNCs for highly efficient LEDs.

While PNCs have exceptional luminescent properties,^[27,28] their widespread application is hindered by their low chemical and colloidal stability.^[29] The intrinsic instability originates from the low energy of lead halide perovskite formation and this includes structures such as CsPbX₃ and MAPbX₃, where X = Cl, Br, and I, and MA = methylammonium cation.^[30] Moreover, the aggregation of PNCs caused by proton exchange reactions between surfactants and passivation ligands leads to the facile detachment of the ligands that provide colloidal stability.^[31,32] This process is often promoted by the perovskite's low crystal formation energy and cation migration under applied bias,^[33,34] shifting and broadening the luminescent peaks and degrading the device performance.

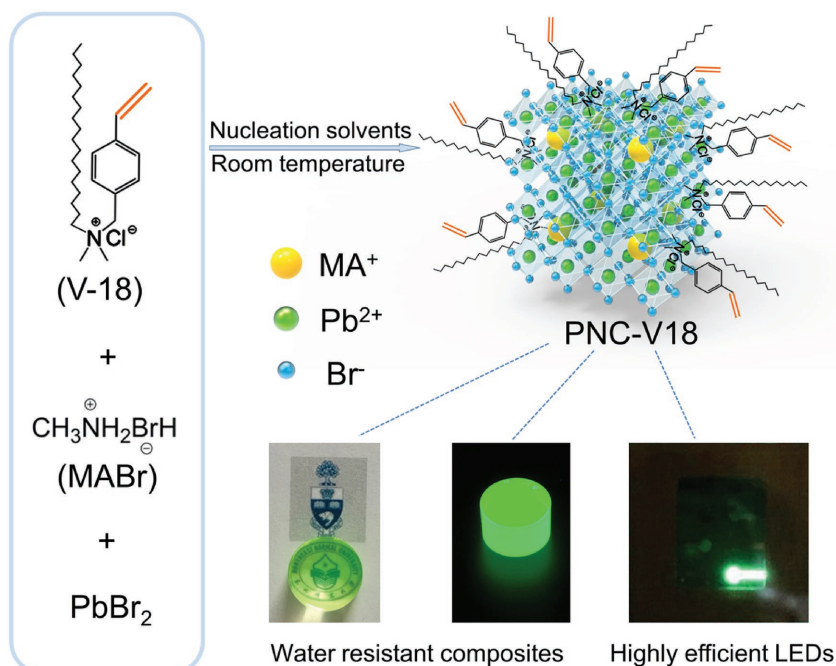
Several methods have therefore been developed to enhance the chemical and colloidal stability of PNCs through ligand and surface engineering. Luo et al. improved the stability of PNCs using branched capping ligands, resulting in an 80% retention of the photoluminescence (PL) intensity after suspension in protic solvents such as isopropanol.^[35] Using polymer matrices can also effectively enhance PNC chemical stability.^[36–38] However, due to the insulating nature of the polymers, the conductivity of PNC thin films is substantially reduced, excluding these materials from use in electroluminescence (EL) applications. Recently, Greenham and co-workers reported efficient PNC LEDs with an atomic-layer-deposited alumina surface passivation layer.^[39] The thin layer of passivating oxide enables efficient charge recombination within individual PNC domains while enhancing device stability. However, this approach does not replace the original oleic acid ligands, and the weak interaction between oleic acid and PNC surfaces will reduce long-term stability.^[32,40] While these reports address individual issues of PNCs for light-emitting applications, a strategy to address both the colloidal and chemical instabilities of PNC without compromising performance remains elusive.

Herein, we introduce a new approach to enhance PNC stability through a class of intrinsically crosslinkable and polymerizable ligands. These ligands contain a styryl group, providing an opportunity for crosslinking and polymerization on the surface of the PNCs. Crosslinking between PNCs is achieved via heating with a radical initiator, which effectively improves the stability of the resultant PNCs. Moreover, a novel bulk polymer–PNC composite is obtained via radical polymerization, and this composite possesses excellent transparency and resistance to water. In comparison with a commonly used stabilizer such as octylammonium bromide (CH₃(CH₂)₇NH₃Br, OABr), the PNCs reported here possess a homogeneous morphology and a high PLQY. We further demonstrate the application of these crosslinked PNCs in LEDs. The best device exhibits a maximum luminance exceeding 7000 cd m⁻², over 300% better than previously reported MA-based PNC devices.^[23] This new strategy and the corresponding

devices incorporating crosslinked PNCs demonstrate the importance that PNC ligand design has on stability and device performance. It also represents a surface modification approach to high-performance, stable, and affordable PNC-based LEDs.

The precursors, ligands, and resultant PNCs used in this study are summarized in **Scheme 1**. We chose to use 4-vinylbenzyl-dimethyloctadecylammonium chloride (V18)-based ligands in this study for three key reasons: first, the ammonium center with two methyl groups allows sufficient ionic interaction with the perovskite surface; second, the styryl group allows for radical polymerization to proceed from the surface ligand as well as crosslinking between two adjacent nanocrystals; finally, the alkyl side chain imparts a high colloidal stability for the PNCs. MAPbBr₃ PNCs were prepared using a one-step colloidal synthetic approach under the normal laboratory atmosphere. Briefly, lead bromide (PbBr₂), methylammonium bromide (CH₃NH₃Br, MABr), and V18 were dissolved in dimethylformamide (DMF) to yield the precursor solution. The solution was subsequently injected into the nucleation solvent (either toluene or tetrahydrofuran (THF)) to directly obtain PNCs passivated by a mixture of V18 and MABr ligands. Once the residual organic ligands were removed (see the “Experimental Section”), the isolated PNCs showed homogeneous morphology and high PLQY (≈100% in solution and up to 56% in film).

By adjusting the halide component (i.e., Cl:Br) through variation of the V18:MABr ratio, the PL emission peak of the PNCs is readily tuned (**Figure 1a**). The narrow emission peak, with no shoulder peaks, shifts from 482 to 508 nm when the molar ratio of V18 to MABr changes over a range from 6:4 to 3:7, with high PLQYs ranging from 75% to ≈100%. The UV–vis absorption spectra of the various PNC samples (Figure S1,



Scheme 1. The design of PNCs modified with chemically addressable ligands and their application in LEDs and as water-resistant composites.

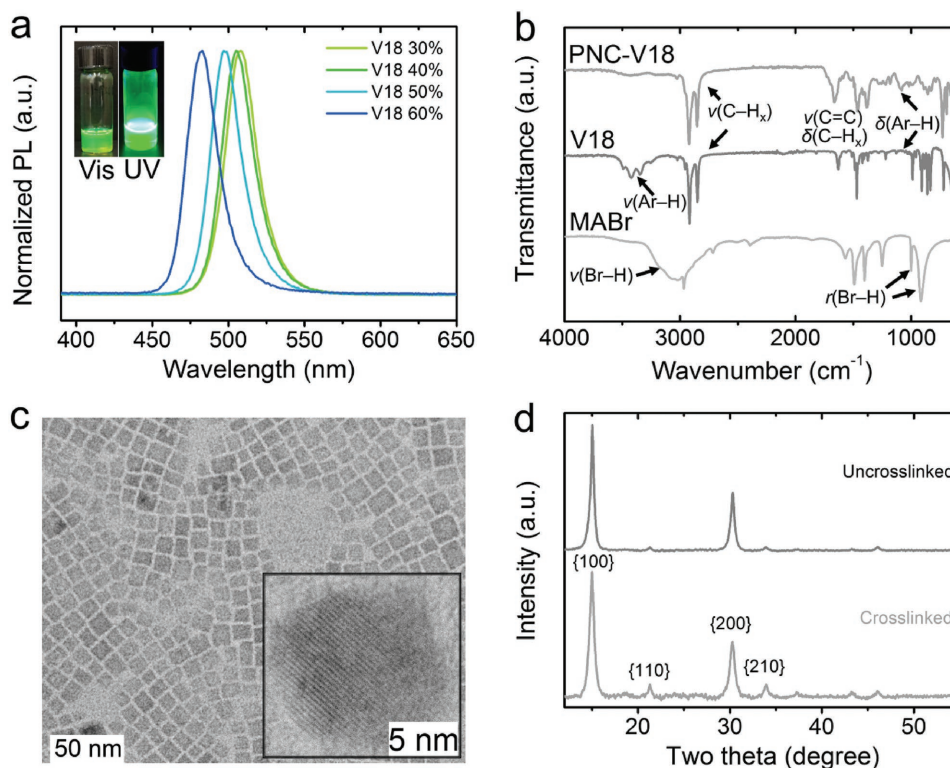


Figure 1. a) PL spectra of PNC-V18 with different molar ratios of V18. Insets are the photos of the PNC-V18 solution under ambient room lighting and UV illumination. b) FTIR spectra of PNC-V18, ligand V18, and MABr, showing that V18 has been successfully attached on the surface of PNCs. c) TEM image of PNC-V18. Inset is the HRTEM image of PNC-V18. d) XRD pattern of PNC-V18 as prepared and crosslinked.

Supporting Information) have single exciton absorption peaks ranging from 443 to 499 nm. A solution of the PNCs exhibits bright green fluorescence even under ambient room lighting (Figure 1a, inset). The PL spectra of all PNC samples have a narrow full width at the half-maximum (FWHM) in the range of 25 nm. The Stokes shifts are only ≈ 15 nm, implying that the PL emission mainly results from the exciton recombination. This confirms that all PNCs with different V18-to-MABr ratios show high PLQYs, whereas their physical properties, such as solution processability and film conductivity, are different. The increase of long chain ligands (V18:MABr = 6:4 and 5:5) enables sufficient ligand passivation on PNC surfaces and enhances solubility. However, large loadings of V18 may introduce excess surface-capped ligands due to ligand-ligand van der Waals interaction. The presence of excess ligand molecules impairs the charge carrier transport and injection to the PNC active layer, and negatively affects the device performance. On the other hand, PNC solubility is decreased as the V18:MABr precursor ratio is reduced, which substantially affects the film morphology and hence the device performance. The selection of PNCs with specific V18:MABr ratio (i.e., 4:6, both has high PLQY of 95% and high solubility of 4 mg mL^{-1} in THF) is therefore based on the overall consideration of film PLQY, film morphology, and conductivity. All later investigations will focus on this sample, abbreviated as PNC-V18 for clarity. In addition, the lifetimes of PNC-V18 solution are 7.3 and 36.1 ns, where τ_1 is attributed to the intrinsic recombination while τ_2 comes from surface state recombination (Figure S2,

Supporting Information). For comparison, PNCs with OABr as ligands (PNC-O8) were synthesized using the same procedure (V18 ligands were replaced by OABr). In this control sample, we observe three absorption peaks at 453, 470, and 515 nm, indicating that emission is not exclusively arising from exciton recombination (Figure S3, Supporting Information).^[41,42] Correspondingly, the PL spectrum has three emission peaks and the PLQY is only 38%, which is much lower than PNC-V18.

The attachment of V18 on PNC surfaces was examined by Fourier transform infrared (FTIR) spectroscopy (Figure 1b). The FTIR spectrum of MABr has three strong characteristic signals at $2700\text{--}3300 \text{ cm}^{-1}$ (broad), $\approx 1000 \text{ cm}^{-1}$ (narrow), and $\approx 890 \text{ cm}^{-1}$ (medium), which are assigned to Br-H stretching, C-H_x rocking (MA translation), and C-H_x rocking (MA rotation), respectively.^[43] The disappearance of these MABr characteristic broad signals at $2700\text{--}3300 \text{ cm}^{-1}$ from the spectrum of PNC-V18 indicates no residual MABr is present in the purified PNC sample. On the other hand, V18-passivated PNCs exhibit intense absorptions at 2925 and 2853 and $1300\text{--}1500 \text{ cm}^{-1}$ (Figure S4, Supporting Information), that are attributed to the C-H stretching and bending vibration of alkyl groups on V18 ligands, respectively. The peaks at 1611 and 1513 cm^{-1} , 1477 and 1423 cm^{-1} are attributed to the C=C stretching vibrations of the aromatic rings, and these are found in both the spectra of the free V18 ligands and passivated PNCs (Figure S4, Supporting Information). The weak absorption characteristics of in-plane and out-of-plane C-H_x bending arising from aromatic rings on V18 are observed between 700 and 1200 cm^{-1} .

The C=C stretching signal is observed at 1633 cm^{-1} in the spectrum of freshly prepared PNC sample (Figure S4, Supporting Information).

The uniform morphology and size distribution of PNC-V18 are revealed by electron microscopy. Transmission electron microscopy (TEM) images (Figure 1c) reveal that PNC-V18 is composed of well-defined nanocubes with a side length of $\approx 10\text{ nm}$. Note that there are no other co-ligands such oleic acid or oleic amine in the system; therefore, the V18 ligand indeed appears to have a favorable influence on the homogeneity and size distribution of PNCs. X-ray diffraction (XRD) experiments show the strong scattering signals that are consistent with an MAPbX_3 perovskite crystal (Figure 1d).^[17] The features at 15° , 21° , 30° , and 34° are assigned to the {100}, {110}, {200}, and {210} lattice planes of an MAPbX_3 structure, respectively.^[44]

The presence of the vinyl surface groups allows the PNC-V18 samples to be crosslinked, and a variety of experiments were carried out to understand how this affects their properties. Here, crosslinking was accomplished by heating the PNC-V18 samples in the presence of azobisisobutyronitrile (AIBN) at 90°C under an inert atmosphere for 30 min (see the “Experimental Section”). Chemical evidence that crosslinking has taken place is observed in the FTIR spectrum, where the C=C stretching signals disappear after crosslinking (Figure S5, Supporting Information). After crosslinking, no narrowing/broadening or shifting of any crystalline signals is observed (Figure 1d). The samples have very similar absorption spectra (Figure S6, Supporting Information), size and shape (Figure S7, Supporting Information) before and after crosslinking. These results indicate the size, crystallinity, and optical properties of PNCs are retained upon crosslinking.

Survey X-ray photoelectron spectra (XPS) indicate that the PNCs contain only the elements expected in the perovskite and V18 ligands (Figure S8a and S9a, Supporting Information) before and after crosslinking. High-resolution XPS analysis further confirms the elemental composition of PNC-V18: lead (4f) at 138.6 and 143.5 eV, bromine (3d) at 68.3 eV, chlorine (2p) at 197.9 eV, carbon (1s) at 284.9 eV, and nitrogen (1s) at 402.1 eV.^[45] Similar to the XRD results, the XPS signals remain unchanged after crosslinking (Figure S8 and S9, Supporting Information), reflecting the fact that crosslinking does not change the chemical composition of PNC-V18. The atomic ratios of Pb to [Br + Cl] are 1:3.2 and 1:3.1 for the sample before and after crosslinking, respectively. The appropriate excess of halogen atoms present on the surface of the PNCs is expected to favor the passivation of PNCs, and therefore, improves their PLQYs.^[46]

The properties of the PNC thin-film determine eventual performance in optoelectronic applications. We obtained transparent PNC-V18 thin films by spin-casting with and without crosslinking. Before crosslinking, the film has a strong excitonic and an emission signal at 493 and 512 nm with the PLQY of 33% (Figure 2a; Figure S6, Supporting Information). Compared with the solution-based samples (Figure 1a; Figure S1, Supporting Information), both the excitonic peak and the emission peak shift to a slightly longer wavelength in the film (within 7 nm). The small Stokes shift of the PNC-V18 film (only 19 nm) implies that the PL emission mainly results from exciton recombination. Strikingly, the PLQY is improved to

56% upon crosslinking (Figure 2a). When the same experiment was carried out with the control sample (PNC-O8), the transparency of the film is reduced after annealing (Figure S10, Supporting Information). Additionally, the PLQY of PNC-O8, which began at around 32%, drops to 11% after heat treatment (Figure S11, Supporting Information). This shows that the improved luminescent properties are achieved through the surface passivation by crosslinkable ligands.

We attribute the improvement of PLQY to the decreased surface defect density of PNCs after crosslinking, which is supported by a longer Auger recombination process observed in ultrafast transient absorption (TA) spectroscopy (Figure 2b,c). The Auger recombination process shows 38% increase (i.e., from 104 to 143 ps). The decreased surface defect density is further proved by time-resolved PL spectroscopy, which indicates longer PL decay in the crosslinked PNC film. The PL lifetimes (τ_1 , τ_2) of PNC-V18 before and after crosslinking is (5.8 and 23.7 ns) and (7.6 and 31.7 ns), respectively (Figure 2d; Table S1, Supporting Information). The shorter one is attributed to the intrinsic recombination while the longer one comes from surface state recombination. The lifetime for the intrinsic recombination is improved by 31%, and that for the surface state recombination is improved by 34%.

The decomposition temperature of the as-prepared PNC-V18 is 295°C , indicating excellent thermal stability (Figure S12, Supporting Information). After crosslinking, in addition to the maintenance of crystal structure and morphology (Figure 1d; Figure S7, Supporting Information), no change in PL intensity versus time was found after storing the film in the laboratory atmosphere for 30 d and both the peak shape and position do not change (Figure 2e; Figure S13, Supporting Information). This is in contrast to the PNC-V18 that is not crosslinked, which maintained 85% of the PL intensity under the same conditions. For comparison, only $\approx 65\%$ PL intensity was maintained for the film of PNC-O8 (Figure 2e). These results further highlight the outstanding properties imparted by the crosslinked V18 ligands on the surface of the PNCs.

To measure the electroluminescent properties of these novel PNCs, we fabricated LEDs with an inverted structure (Figure 3a) in which the PNC layer was sandwiched between the electron transport layer (ETL; TiO_2 nanoparticle (NP) layer + atomic layer deposition (ALD) processed Al_2O_3 thin layer) and the hole transport layer (HTL) poly(9,9'-dioctylfluorene) (F8). The PNC-V18 solution with the AIBN radical initiator was spin-cast directly onto the ETL-coated substrates, and subsequently annealed to initiate the crosslinking reaction. To avoid the formation of pin holes caused by shrinkage of PNC thin film upon crosslinking, we applied a two-step spin-casting/polymerization process to prepare the crosslinked PNC active layer (see the “Experimental Section”). Ultraviolet photoelectron spectra (UPS) show that the valence band is located at -6.8 eV relative to vacuum, while the conduction band is located at -4.4 eV (Figure S14, Supporting Information). The conduction band and the valence band for PNC-V18 before crosslinking are located at -4.5 and -6.9 eV , respectively. These results show that crosslinking induced energy level shift, which was also observed in other investigations.^[41,47] As a result, the energy band offset between the PNCs and the HTL was reduced for our

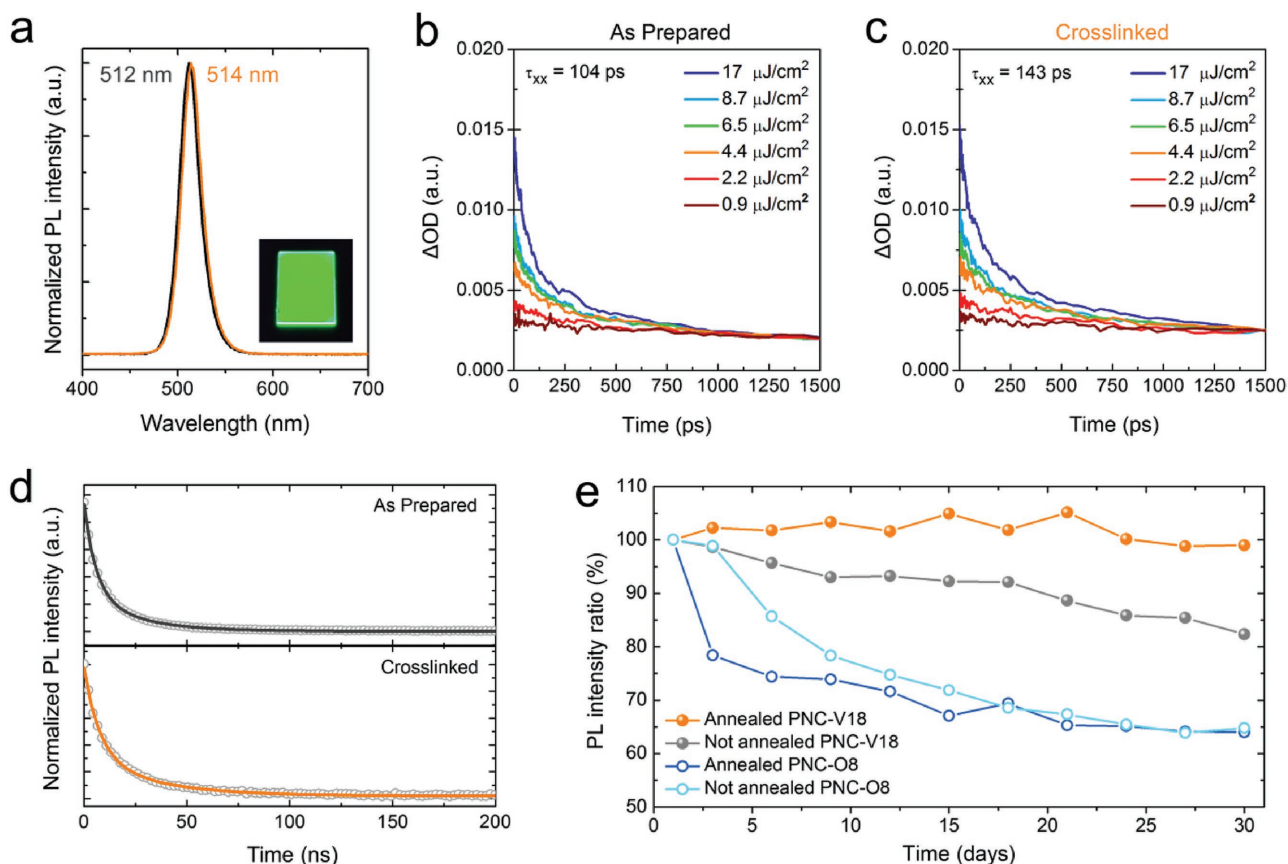


Figure 2. a) PL spectra of PNC-V18 film as prepared (black line) and crosslinked (orange line). The inset is the photo of the film, showing homogeneous green emission. b) TA spectra of PNC-V18 as prepared and c) crosslinked, indicating that the surface defects of PNCs decrease after crosslinking. d) PL decay of PNC-V18 film as prepared (black line) and crosslinked (orange line). e) Stability of the different films for 1 month. Approximately 100% of PL intensity is remained for the crosslinked PNC-V18 film; 85% is remained for the as prepared PNC-V18 film, and only $\approx 65\%$ is remained for the PNC-O8 film with and without annealing, indicating good stability of the crosslinked PNC-V18 film.

devices and consequently leads to good EL performance.^[47] In Figure 3b, the band diagram of the LEDs shows the alignment of the band levels between the active PNCs and carrier transfer materials. The conduction band minimum of chloride-capped TiO₂ NPs is lower than the sol-gel processed TiO₂ layer,^[48] and exactly aligns with the valence band minimum of the PNC-V18 layer. We applied a thin layer of Al₂O₃ (2 nm) to reduce the electron injection rate and achieve the balance of charge carrier injection. The cross-sectional scanning electron microscopy image confirms the thickness of each component: TiO₂ NPs + Al₂O₃: 65 nm, crosslinked PNCs' layer: 42 nm, F8: 30 nm, and MoO₃: 6 nm + Ag: 100 nm (Figure 3c). Atomic force microscopy (AFM) reveals a low surface roughness (root mean square (RMS) roughness = 3.8 nm) and a pin-hole-free active layer after the two-step spin-casting/annealing process (Figure S15, Supporting Information).

The EL spectrum of perovskite NC device under the applied bias of 5 V is shown in Figure 3d. The EL signal is symmetric and the emission peak occurs at 528 nm, an ≈ 14 nm redshift from the thin-film PL result. No peak broadening was observed in the devices; the FWHM values of EL and PL signals are 24 and 25 nm, respectively. This indicates the EL quality of the PNC-V18 device is very high and well preserved after solution

processing, crosslinking, and device fabrication. The low device turn-on voltage of ≈ 3 V indicates efficient charge carrier injection from the charge transport layers to the crosslinked PNC layer (Figure 3e). The low current density (CE) under the bias below device turn-on voltage confirms that the Al₂O₃ layer successfully balances carrier injection and efficiently blocks hole carriers. Because the thin and robust polymer shell effectively protects labile PNC surfaces and maintains good charge transport, these LEDs operated substantially more efficiently than reported MAPbX₃ PNC devices (Table S2, Supporting Information), and showed enhanced stability at practical operating voltages. The maximum luminance was over 7200 cd m⁻² at the applied voltage of 9 V. This surpasses the luminance of previously reported MAPbX₃ nanocrystal-based devices by around threefold with a substantially improved device breakdown voltage.^[23] The maximum EQE and CE were 0.58% and 2.47 Cd A⁻¹ at the applied bias of 8 V (Figure 3f). More importantly, these crosslinked devices maintain high performance (CE > 2 Cd A⁻¹; luminance > 7000 cd m⁻²) at an operational voltage up to 9 V, over 400% CE improvement over previous MAPbX₃-based LEDs^[23] (the latter exhibited CE of ≈ 0.4 Cd A⁻¹ at the breakdown bias of ≈ 7 V) (Table S2, Supporting Information). All of these device metrics show that

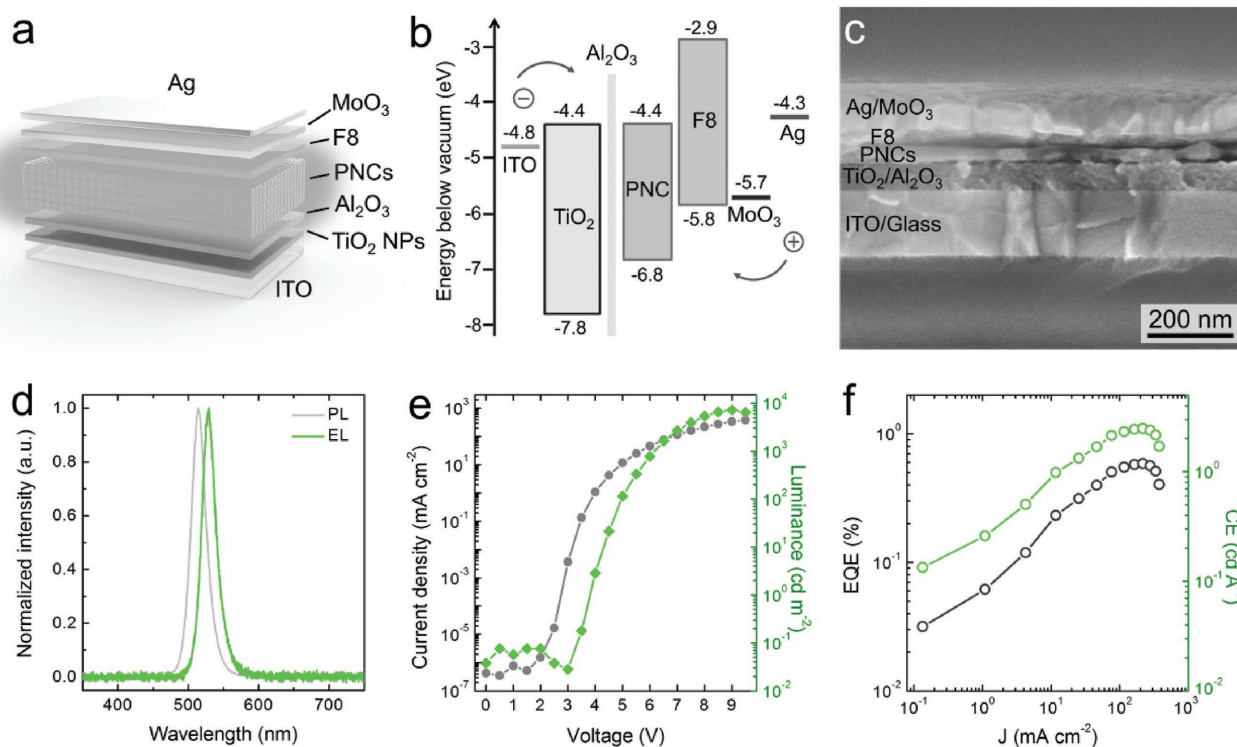


Figure 3. a) Structure of the LED device. b) Energy diagram of the LED device showing the alignment of the band levels between the active PNCs and carrier transfer materials. c) Cross-sectional SEM image of the device, confirming the thickness of each component. d) PL and EL spectra of the PNC-V18 thin film and the LED device, confirming an ≈ 14 nm redshift from the thin-film PL result. e) J - V and luminance curves of the LED device, showing the low turn-on voltage and high luminance. f) EQE and CE curves of the LED devices.

the robust interaction between crosslinkable ligands and PNC surfaces improves performance and stability, and represents a promising step toward manufacturable, high-performance PNC-based LEDs.

In addition, the moisture stability of PNC-V18 is investigated. In Figure S16 (Supporting Information), it is shown that about 85% of PL intensity was remained after PNC-V18 with crosslinking was put into water for about 120 min while about 72% of PL intensity was remained for PNC-V18 without crosslinking. Both cases show that PNC-V18 has some degree of water resistance, although they exhibit a decrease in PL intensity after exposure to water. Note that the styryl surface ligand makes it possible to incorporate PNC-V18 into a polymer matrix by copolymerization with styrene and methyl methacrylate (MMA) via radical polymerization. We take advantage of this property to further improve water resistant. Briefly, the purified PNC solid was distributed in the mixture of styrene and MMA (e.g., with the volume ratio of 1:3), followed by introducing the AIBN initiator (0.5% of monomer), and then the polymerization was carried out under the protection of inert gas at 65 °C for 50 h. The PL spectrum of the polymer composite shows strong PL emission at 522 nm (Figure 4a, black line). The peak shape of the PNC-V18 is well preserved after copolymerization with styrene and MMA. The composite material also has good processability, and it can be molded into a cylinder, cube, and triangular prism, etc (Figure 4b). The bulk composite has excellent transparency, which indicates good compatibility between PNC-V18 and the polymer matrix

(Figure 4b). More importantly, the composite is water resistant with almost no change in PL after the material was immersed in water for 90 d (Figure 4a,c).

In summary, we have developed the first synthesis of PNCs with crosslinkable and polymerizable ligands. We show that this enhances PNC surface passivation, and simultaneously provides high film conductivity and optical homogeneity for optoelectronic applications. The ligands contain styryl groups, which are a convenient chemical handle for crosslinking via heat treatment and a radical initiator or polymerization with other monomers using radical-based methods. The synthesis of these novel PNCs does not use high-boiling-point solvents (such as octadecene), excess stabilizing agents (such as oleic amine or oleic acid), heating, or inert gas protection. The obtained PNCs possess homogeneous morphology and high PLQY. The PNCs can be copolymerized with styrene and MMA to obtain homogenous hybrid materials that have excellent resistance to water. The application of crosslinked PNCs in LEDs was demonstrated. The best device exhibits a maximum luminance exceeding 7000 cd m^{-2} , over 300% better than previous reported MA-based PNC devices. This work shows that ligand design is of utmost importance for materials' stability and device performance. This appears to be a very promising approach toward high-performance and stable PNC LEDs and should be broadly applicable to other perovskite optoelectronic devices including solar cells, photodetectors, and lasers, where stability issues hinder the widespread use of these technologies.

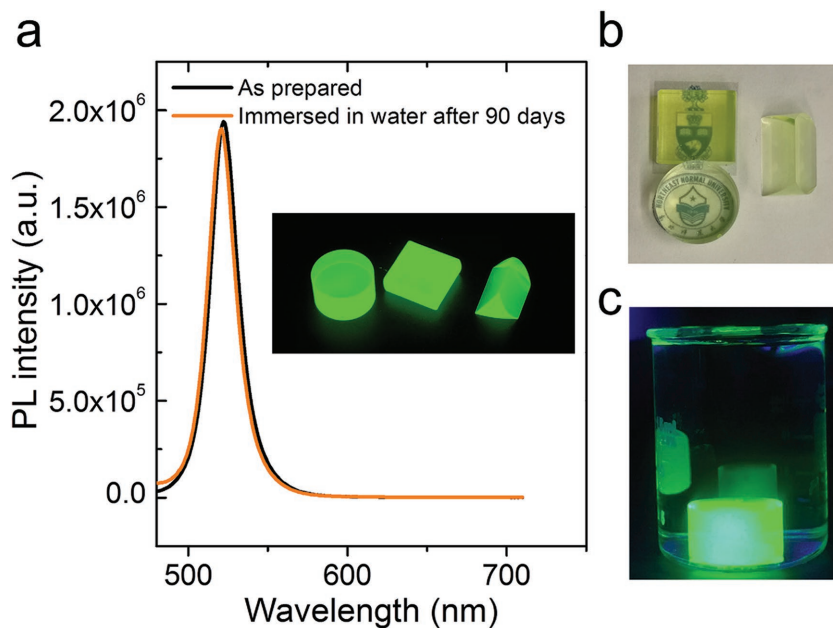


Figure 4. a) PL spectra of the PNC-V18-polymer composite. The black line is the PL spectrum of the as-prepared composite; the orange line is the PL spectrum of the composite immersed in water for 90 d, indicating that the composite possesses good water resistivity. The inset is the photo of bulk material under UV illumination, showing bright green fluorescence. b) The bulk composite has good transparency. c) The photo of the bulk composite immersed in water at the 90th day shows that it still possesses the same emission properties.

Experimental Section

Materials: Lead bromide (PbBr_2) (99%), methylamine, octylamine, hydrobromic acid (HBr) (48% in water), AIBN, MMA, styrene and 4-vinylbenzyl chloride (99%), titanium tetrachloride (TiCl_4) (99.9%), benzyl alcohol (anhydrous, 99.8%), trimethylaluminum (97%), and poly(9,9-di-*n*-octylfluorenyl-2,7-diyl) (F8) ($M_w > 20\,000\text{ g mol}^{-1}$) were purchased from Sigma-Aldrich. *N,N*-dimethyloctadecylamine (89%) was purchased from Acros. DMF, toluene, chlorobenzene, THF, acetone, ethanol, diethyl ether, and 1-butanol were used as received.

Synthesis: Methylammonium bromide ($\text{CH}_3\text{NH}_3\text{Br}$) and octylammonium bromide ($\text{CH}_3(\text{CH}_2)_7\text{NH}_3\text{Br}$) were prepared via the reaction of the corresponding amine in water/HBr, accordingly to a previously reported procedure.^[23,26] Briefly, 6 mL of methylamine and 10 mL of HBr were added into a 100 mL three-neck flask at 0 °C. After 2 h of stirring, the solvents were removed by rotary evaporation until a white precipitate was obtained. The precipitate was dissolved in a small amount of ethanol, followed by recrystallizing from diethyl ether, and dried at room temperature under vacuum oven for 24 h. OABr was prepared via a similar process.

Synthesis of 4-Vinylbenzyl-dimethyloctadecylammonium Chloride: The polymerizable surfactant V18 was prepared according to ref. [49]. *N,N*-dimethyl-octadecylamine (4.2 mL) was dissolved in acetone (5 mL), and 4-vinylbenzyl chloride (9 mL) was added dropwise to the solution. The mixture was heated at 40 °C for 2 h under reflux. Then, the mixture was washed with acetone many times, followed by extraction filtration and dried under vacuum for 24 h. NMR (CDCl_3): 0.87–0.89 (m, 3 H, CH_2CH_3), 1.26–1.32 (t, 32 H, CH_2), 3.31 (s, 6 H, $\text{CH}_3\text{-N-CH}_3$), 3.47–3.51 (m, 2 H, $\text{CH}_2\text{CH}_2\text{-N}$), 5.09 (s, 2 H, arom- $\text{CH}_2\text{-N}$), 5.35–5.83 (2 s br, 2 H, $\text{CH}=\text{CH}_2$), 6.68–6.74 (m, 1 H, $\text{CH}=\text{CH}_2$), 7.44–7.63 (2 s br, 4 H, aromatic).

Synthesis of PNCs: The PNCs were prepared by dissolving a specified amount of PbBr_2 , MABr, and V18 (or OABr) in DMF separately. (Note: PbBr_2 and V18 were heated at 80 °C to ensure complete dissolution.)

Then, the three solutions were mixed together and added into nucleation solvent (toluene or THF). The solution turned green immediately, indicating the formation of PNCs. As an example, PNC-V18 with a V18-to-MABr ratio equal to 4:6 was synthesized by dissolving PbBr_2 (0.0367 g), V18 (0.0180 g), and MABr (0.0066 g) in DMF (100 μL), respectively. After complete dissolution, the solutions were mixed together and added into 6 mL of toluene. For the purification of PNCs, the above solution was centrifuged at 4400 rpm for 10 min. The precipitate was discarded, and the supernatants were washed with 1-butanol twice to remove the excess organic ligands, and dried under vacuum for 24 h.

Synthesis of PNC-Polymer Bulk Composite: Styrene (ST) (1 mL) containing PNCs (0.5 mg mL^{-1}) was mixed with MMA (3 mL). Then, AIBN (0.02 g) was added into the monomer solution. The solution was degassed at 77 K for 15 min, and inert gas was bubbled through the system for 15 min. This procedure was repeated five times. The polymerization was carried out at 65 °C for 50 h.

Stability of PNC Film: PNC-V18 was dissolved in THF (4 mg mL^{-1}). The solution was filtered using a 0.45 μm filter to obtain a bright green solution. The solution was then spin-coated (2500 rpm, 30 s) onto a glass substrate in air. The obtained film was placed in the air, and PL measurements were taken regularly. For the crosslinked film, PNC-V18 was dissolved (4 mg mL^{-1}) in an AIBN:THF solution (concentration of AIBN: 0.1–0.2 mg/6 mL). After filtration, the solution was then spin-coated (2500 rpm, 30 s) onto a glass substrate in air and then annealed at 90 °C for 30 min in an Ar-filled glovebox to form the crosslinked PNC film.

Material Characterizations of PNCs: Absorption spectra were recorded on a Varian Cary 5000 UV-vis-NIR spectrophotometer. Thermal gravity analysis was obtained with a Q500 thermogravimetric analyzer (American TA Company). Photoluminescence measurements were performed using a Horiba Fluorolog Time Correlated Single Photon Counting system with photomultiplier tube detectors. A monochromatized Xe lamp and pulsed laser diodes (442 nm) were used as excitation sources for steady-state measurements. Absolute PLQY measurements for the liquid samples were carried out using an integrating sphere according to the method published elsewhere.^[50] TEM and HRTEM images were obtained on a JEOL2010 high-resolution TEM (HRTEM) microscope at an accelerating voltage of 200 kV. XRD patterns were collected using a Rigaku MiniFlex 600 diffractometer equipped with an NaI scintillation counter and using monochromatized $\text{Cu K}\alpha$ radiation ($\lambda = 1.5406\text{ \AA}$). XPS analysis was carried out using the ThermoFisher Scientific K-Alpha XPS system. The energy band value was measured in an integrated ultrahigh vacuum system equipped with multitechnique surface analysis system (VG ESCALAB MK II spectrometer). UPS was measured with the He (I) (21.2 eV) line using a negative bias voltage applied to the samples in order to shift the spectra from the spectrometer threshold.

Time-Resolved Photoluminescence Spectroscopy: Time-resolved photoluminescence spectroscopy measurements were performed using the Horiba Fluorolog Time-Correlated Single Photon Counting (TCSPC) system equipped with UV/vis/NIR photomultiplier tube detectors, dual grating spectrometers, and a monochromatized xenon lamp excitation source. The film was placed at an incident angle of 30° away from the detector to avoid reflections of the incident beam. A 375 nm laser diode was used as a pulsed excitation source, and the time traces were acquired using the TCSPC near-infrared detector. The time window was set appropriately to ensure a complete decay of the photogenerated carriers.

Ultrafast TA Spectroscopy: Femtosecond laser pulses of a 1030 nm fundamental beam at a 5 kHz repetition rate were produced using a

regeneratively amplified Yb:KGW laser (PHAROS, Light Conversion). Part of the fundamental beam was used to pump an optical parametric amplifier (ORPHEUS, Light Conversion) to serve as a narrowband pump, while the other part was focused into a sapphire crystal to generate a white-light supercontinuum probe which was set near the position of the first absorption peak. Both the pump and probe pulses were directed into a commercial transient absorption spectrometer (Helios, Ultrafast). Delaying the probe pulse relative to the pump provides a time window of up to 8 ns, and the time resolution of these experiments was ~300 fs (estimated by the rise time of signal amplitudes in transient absorption spectra). TA measurements on PNC films were performed to extract Auger lifetimes and dynamics. The films were pumped at 3.1 eV, and the pump intensity per cm² was measured based on the laser power and spot size. For the lowest pump intensity, no Auger decay signature was observed. To extract Auger lifetime, it was assumed that all the multiexcitons were decayed at 1500 ps. The amplitude of decay at 1500 ps was then normalized to the same value for all pump intensities. After normalization, the high-pump-intensity trace whose maximum amplitude was twice larger than that of the lowest-pump-intensity trace was chosen for lifetime fitting. Exponential decay function with two decay times was used for fitting. This way, the faster decay time corresponded to the Auger lifetime τ_{ex} .

Fabrication of LEDs: TiO₂ NPs were synthesized and purified following the previously reported approach.^[48] These NPs were spin-cast (3000 rpm, 30 s) on prepatterned indium tin oxide (ITO)-coated glass substrates, and the films were annealed in air at 120 °C for 30 min. The Al₂O₃ layer (2 nm) was fabricated by the disposition at 150 °C with ALD (Cambridge Savannah S100 ALD system) using trimethylaluminum and water as precursors. Once cool down, the substrates were stored in an N₂-filled glovebox for further use.

For the film formation and crosslinking reaction, purified PNCs (20 mg) were redispersed into AIBN THF solution (the concentration of AIBN: 0.1–0.2 mg/6 mL, 3 mL). The solution was then spin-coated (3000 rpm, 30 s) onto the TiO₂/Al₂O₃ substrates in air and then annealed at 90 °C for 30 min in an N₂-filled glovebox to form the first layer of the crosslinked PNC film. Then the substrates were transferred outside the glovebox, and the second layer of the PNC/AIBN THF solution was spin-cast onto the substrate with the same spin speed (i.e., 3000 rpm, 30 s). The substrates were subsequently transferred back to the N₂-filled glovebox and annealed at 90 °C for 30 min to complete the crosslinking reaction.

The HTL material F8 was fully dissolved in chlorobenzene (10 mg mL⁻¹) under overnight stirring at 70 °C under an inert atmosphere. Once cool down, the solution was stored in an N₂-filled glovebox for further use. For the formation of HTL, F8 chlorobenzene solution was spin-cast (spin speed: 3000 rpm for 60 s) onto the crosslinked PNC layer. The top electrode, consisting of 10 nm of MoO₃ and 120 nm of Ag, was deposited by thermal evaporation at a pressure of <1 × 10⁻⁶ Torr. Each ITO substrate (2.5 cm × 2.5 cm) was patterned to yield eight devices, each with an active area of 4.9 mm².

PLQY of Film and EL Measurements: Absolute PLQY measurements were done in a Quanta-Phi integrating sphere according to the standard method published elsewhere.^[51] For EL measurement, devices were characterized using a Keithley 2410 source meter. Under a range of forward bias voltages, the EL spectra were collected through a set of lenses focused on an optical fiber and connected to a visible light spectrophotometer (Ocean Optics, USB2000).

Device Performance Characterization: The radiated power of EL was measured using a calibrated Ophir PD300-3W photodiode and recorded in situ by a computer-controlled Keithley 2400 source meter under nitrogen atmosphere and in parallel with the current–voltage (*I*–*V*) measurements. Lambertian emission was assumed in the calculation of EQE and luminance. Peak EQE was determined as the number of forward-emitted photons to the number of injected electrons. A geometry correction factor was used according to the distance between photodiode and device and the active area of the detector.

AFM and Scanning Electron Microscopy (SEM) Measurements: AFM was carried out using an Asylum Research Cypher system. The AFM was

operated in AC mode in air to obtain topographical and phase images. Silicon ASYELEC-01 probes with titanium–iridium coatings from Asylum Research were used for all imaging. Probes typically have a spring constant of 2 N m⁻¹. Cross-sectional SEM images were obtained from a field-emission scanning electron microscope (Hitachi SU8230) with an operational voltage of 3 kV.

Supporting Information

Supporting Information is available from the Wiley Online Library or from the author.

Acknowledgements

H.S. and Z.Y. contributed equally to this work. This work was supported by the Ontario Research Fund Research Excellence Program, the Natural Sciences and Engineering Research Council (NSERC) of Canada, the Canadian Foundation for Innovation, DuPont, an award (KUS-11-009-21) from the King Abdullah University of Science and Technology (KAUST), and the A. P. Sloan Foundation. H.S. acknowledges the support of National Natural Science Foundation of China (NSFC) (21574018 and 51433003) and China Scholarship Council (CSC). W.S. and G.A.O. acknowledge the support of Connaught Innovation Fund and Connaught Global Challenge Fund. H.T. acknowledges the Netherlands Organisation for Scientific Research (NWO) for a Rubicon grant (680-50-1511) to support his postdoctoral research at University of Toronto. The authors appreciate the valuable suggestions of N. Coombs and I. Gourevich for the TEM and HRTEM measurement. The authors thank Dr. F. Fan, Dr. M. Liu, Dr. L. Levina, E. Palmiano, and D. Kopilovic for their help during the course of the study.

Conflict of Interest

The authors declare no conflict of interest.

Keywords

crosslinking reaction, double bond modification, light-emitting diodes, nanocrystals, perovskites, water resistant

Received: February 27, 2017

Revised: June 2, 2017

Published online: July 10, 2017

- [1] NREL Chart, <https://www.nrel.gov/pv/assets/images/efficiency-chart.png>; Accessed: June 2017.
- [2] S. Yakunin, M. Sytnyk, D. Kriegner, S. Shrestha, M. Richter, G. J. Matt, H. Azimi, C. J. Brabec, J. Stangl, M. V. Kovalenko, W. Heiss, *Nat. Photonics* **2015**, *9*, 444.
- [3] H. Wei, Y. Fang, P. Mulligan, W. Chuirazzi, H.-H. Fang, C. Wang, B. R. Ecker, Y. Gao, M. A. Loi, L. Cao, J. Huang, *Nat. Photonics* **2016**, *10*, 333.
- [4] G. Xing, N. Mathews, S. S. Lim, N. Yantara, X. Liu, D. Sabba, M. Grätzel, S. Mhaisalkar, T. C. Sum, *Nat. Mater.* **2014**, *13*, 476.
- [5] Y. Wang, X. Li, J. Song, L. Xiao, H. Zeng, H. Sun, *Adv. Mater.* **2015**, *27*, 7101.
- [6] Z.-K. Tan, R. S. Moggaddam, M. L. Lai, P. Docampo, R. Higler, F. Deschler, M. Price, A. Sadhanala, L. M. Pazos, D. Credgington,

- F. Hanusch, T. Bein, H. J. Snaith, R. H. Friend, *Nat. Nanotechnol.* **2014**, *9*, 687.
- [7] S. D. Stranks, H. J. Snaith, *Nat. Nanotechnol.* **2015**, *10*, 391.
- [8] Y.-H. Kim, H. Cho, J. H. Heo, T.-S. Kim, N. Myoung, C.-L. Lee, S. H. Im, T.-W. Lee, *Adv. Mater.* **2015**, *27*, 1248.
- [9] G. Li, Z.-K. Tan, D. Di, M. L. Lai, L. Jiang, J. H.-W. Lim, R. H. Friend, N. C. Greenham, *Nano Lett.* **2015**, *15*, 2640.
- [10] J. Song, J. Li, X. Li, L. Xu, Y. Dong, H. Zeng, *Adv. Mater.* **2015**, *27*, 7162.
- [11] M. Yuan, L. N. Quan, R. Comin, G. Walters, R. Sabatini, O. Voznyy, S. Hoogland, Y. Zhao, E. M. Bearegard, P. Kanjanaboos, Z. Lu, D. H. Kim, E. H. Sargent, *Nat. Nanotechnol.* **2016**, *11*, 872.
- [12] B. R. Sutherland, E. H. Sargent, *Nat. Photonics* **2016**, *10*, 295.
- [13] N. Wang, L. Cheng, R. Ge, S. Zhang, Y. Miao, W. Zou, C. Yi, Y. Sun, Y. Cao, R. Yang, Y. Wei, Q. Guo, Y. Ke, M. Yu, Y. Jin, Y. Liu, Q. Ding, D. Di, L. Yang, G. Xing, H. Tian, C. Jin, F. Gao, R. H. Friend, J. Wang, W. Huang, *Nat. Photonics* **2016**, *10*, 699.
- [14] S. A. Veldhuis, P. P. Boix, N. Yantara, M. Li, T. C. Sum, N. Mathews, S. G. Mhaisalkar, *Adv. Mater.* **2016**, *28*, 6804.
- [15] F. Zhang, H. Zhong, C. Chen, X.-G. Wu, X. Hu, H. Huang, J. Han, B. Zou, Y. Dong, *ACS Nano* **2015**, *9*, 4533.
- [16] J. C. Yu, D. W. Kim, D. B. Kim, E. D. Jung, J. H. Park, A. Y. Lee, B. R. Lee, D. Di Nuzzo, R. H. Friend, M. H. Song, *Adv. Mater.* **2016**, *28*, 6906.
- [17] X. Zhao, B. Zhang, R. Zhao, B. Yao, X. Liu, J. Liu, Z. Xie, *J. Phys. Chem. Lett.* **2016**, *7*, 4259.
- [18] Y. H. Kim, H. Cho, T. W. Lee, *Proc. Natl. Acad. Sci. USA* **2016**, *113*, 11694.
- [19] Y. Shirasaki, G. J. Supran, M. G. Bawendi, V. Bulović, *Nat. Photonics* **2013**, *7*, 13.
- [20] Y. H. Kim, G. H. Lee, Y. T. Kim, C. Wolf, H. J. Yun, W. Kwon, C. G. Park, T. W. Lee, *Nano Energy* **2017**, *38*, 51.
- [21] J. Byun, H. Cho, C. Wolf, M. Jang, A. Sadhanala, R. H. Friend, H. Yang, T. W. Lee, *Adv. Mater.* **2016**, *28*, 7515.
- [22] L. N. Quan, Y. Zhao, F. P. G. Arquer, R. Sabatini, G. Walters, O. Voznyy, R. Comin, Y. Li, J. Z. Fan, H. Tan, J. Pan, M. Yuan, O. M. Bakr, Z. Lu, D. H. Kim, E. H. Sargent, *Nano Lett.* **2017**, *17*, 3701.
- [23] H. Huang, F. Zhao, L. Liu, F. Zhang, X.-G. Wu, L. Shi, B. Zou, Q. Pei, H. Zhong, *ACS Appl. Mater. Interfaces* **2015**, *7*, 28128.
- [24] J. Xing, F. Yan, Y. Zhao, S. Chen, H. Yu, Q. Zhang, R. Zeng, H. V. Demir, X. Sun, A. Huan, Q. Xiong, *ACS Nano* **2016**, *10*, 6623.
- [25] P. Kumar, C. Muthu, V. C. Nair, K. S. Narayan, *J. Phys. Chem. C* **2016**, *120*, 18333.
- [26] H. Cho, S.-H. Jeong, M.-H. Park, Y.-H. Kim, C. Wolf, C.-L. Lee, J. H. Heo, A. Sadhanala, N. Myoung, S. Yoo, S. H. Im, R. H. Friend, T. W. Lee, *Science* **2015**, *350*, 1222.
- [27] Q. A. Akkerman, V. D'Innocenzo, S. Accornero, A. Scarpellini, A. Petrozza, M. Prato, L. Manna, *J. Am. Chem. Soc.* **2015**, *137*, 10276.
- [28] Y. Hassan, Y. Song, R. D. Pensack, A. I. Abdelrahman, Y. Kobayashi, M. A. Winnik, G. D. Scholes, *Adv. Mater.* **2016**, *28*, 566.
- [29] S. Huang, Z. Li, L. Kong, N. Zhu, A. Shan, L. Li, *J. Am. Chem. Soc.* **2016**, *138*, 5749.
- [30] A. Swarnkar, A. R. Marshall, E. M. Sanehira, B. D. Chernomordik, D. T. Moore, J. A. Christians, T. Chakrabarti, J. M. Luther, *Science* **2016**, *354*, 92.
- [31] E. Yassitepe, Z. Yang, O. Voznyy, Y. Kim, G. Walters, J. A. Castañeda, P. Kanjanaboos, M. Yuan, X. Gong, F. Fan, J. Pan, S. Hoogland, R. Comin, O. M. Bakr, L. A. Padilha, A. F. Nogueira, E. H. Sargent, *Adv. Funct. Mater.* **2016**, *26*, 8757.
- [32] J. De Roo, M. Ibáñez, P. Geiregat, G. Nedelcu, W. Walravens, J. Maes, J. C. Martins, I. Van Driessche, M. V. Kovalenko, Z. Hens, *ACS Nano* **2016**, *10*, 2071.
- [33] A. Buin, P. Pietsch, J. Xu, O. Voznyy, A. H. Ip, R. Comin, E. H. Sargent, *Nano Lett.* **2014**, *14*, 6281.
- [34] C. Eames, J. M. Frost, P. R. Barnes, B. C. O'regan, A. Walsh, M. S. Islam, *Nat. Commun.* **2015**, *6*, 7497.
- [35] B. Luo, Y.-C. Pu, S. A. Lindley, Y. Yang, L. Lu, Y. Li, X. Li, J. Z. Zhang, *Angew. Chem., Int. Ed.* **2016**, *55*, 8864.
- [36] Y. Wang, J. He, H. Chen, J. Chen, R. Zhu, P. Ma, A. Towers, Y. Lin, A. J. Gesquiere, S.-T. Wu, Y. Dong, *Adv. Mater.* **2016**, *28*, 10710.
- [37] Q. Zhou, Z. Bai, W.-G. Lu, Y. Wang, B. Zou, H. Zhong, *Adv. Mater.* **2016**, *28*, 9163.
- [38] L. Protesescu, S. Yakunin, M. I. Bodnarchuk, F. Krieg, R. Caputo, C. H. Hendon, R. X. Yang, A. Walsh, M. V. Kovalenko, *Nano Lett.* **2015**, *15*, 3692.
- [39] G. Li, F. W. R. Rivarola, N. J. L. K. Davis, S. Bai, T. C. Jellicoe, F. de la Peña, S. Hou, C. Ducati, F. Gao, R. H. Friend, N. C. Greenham, Z.-K. Tan, *Adv. Mater.* **2016**, *28*, 3528.
- [40] N. C. Anderson, M. P. Hendricks, J. J. Choi, J. S. Owen, *J. Am. Chem. Soc.* **2013**, *135*, 18536.
- [41] S. Bhaumik, S. A. Veldhuis, Y. F. Ng, M. Li, S. K. Muduli, T. C. Sum, B. Damodaran, S. Mhaisalkar, N. Mathews, *Chem. Commun.* **2016**, *52*, 7118.
- [42] P. Tyagi, S. M. Arveson, W. A. Tisdale, *J. Phys. Chem. Lett.* **2015**, *6*, 1911.
- [43] R. D. Waldron, *J. Chem. Phys.* **1953**, *21*, 734.
- [44] C. H. Lu, J. Hu, W. Y. Shih, W. H. Shih, *J. Colloid Interface Sci.* **2016**, *484*, 17.
- [45] J. Pan, L. N. Quan, Y. Zhao, W. Peng, B. Murali, S. P. Sarmah, M. Yuan, L. Sinatra, N. M. Alyami, J. Liu, E. Yassitepe, Z. Yang, O. Voznyy, R. Comin, M. N. Hedhili, O. F. Mohammed, Z. H. Lu, D. H. Kim, E. H. Sargent, O. M. Bakr, *Adv. Mater.* **2016**, *28*, 8718.
- [46] X. Li, Y. Wu, S. Zhang, B. Cai, Y. Gu, J. Song, H. Zeng, *Adv. Funct. Mater.* **2016**, *26*, 2435.
- [47] K. S. Cho, E. K. Lee, W. J. Joo, E. Jang, T. H. Kim, S. J. Lee, S. J. Kwon, J. Y. Han, B. K. Kim, B. L. Choi, J. M. Kim, *Nat. Photonics* **2009**, *3*, 341.
- [48] H. Tan, A. Jain, O. Voznyy, X. Lan, F. P. García de Arquer, J. Z. Fan, R. Quintero-Bermudez, M. Yuan, B. Zhang, Y. Zhao, F. Fan, P. Li, L. N. Quan, Y. Zhao, Z.-H. Lu, Z. Yang, S. Hoogland, E. H. Sargent, *Science* **2017**, *355*, 722.
- [49] H. Sun, H. Zhang, J. Ju, J. Zhang, G. Qian, C. Wang, B. Yang, Z. Y. Wang, *Chem. Mater.* **2008**, *20*, 6764.
- [50] M. L. Mastronardi, F. Maier-Flaig, D. Faulkner, E. J. Henderson, C. Kübel, U. Lemmer, G. A. Ozin, *Nano Lett.* **2012**, *12*, 337.
- [51] J. C. de Mello, H. F. Wittmann, R. H. Friend, *Adv. Mater.* **1997**, *9*, 230.